IJAME
Int. J. of Applied Mechanics and Engineering, 2026, vol.32, No.3, pp.XXX-XXX
DOI: 10.59441/ijame/221546

A SEMI-ANALYTICAL FRAMEWORK FOR TRANSIENT ELECTRO-MHD OIL TRANSPORT IN SUBSURFACE CAPILLARIES

S. Isa[1], M. Oni[2*] and A. Musa[1]
[1]Mathematics, Yobe State University, NIGERIA
[2]Department of Mathematics, Ahmadu Bello University, NIGERIA
E-mail: michaeloni29@yahoo.com

This study presents a semi-analytical model for transient magnetohydrodynamic (MHD) flow with electrokinetic coupling in cylindrical capillaries representing subsurface oil transport pathways. The model incorporates Lorentz force, electric double layer (EDL) effects, constant pressure gradient, and time-dependent momentum in the Navier-Stokes equations. Using the electrokinetic potential and magnetic field parameters, the governing equations are transformed into a Bessel-type form and solved through Laplace transform methods. Analytical expressions for velocity, shear stress, and flow rate are obtained in Laplace domain after which a numerical inversion method based on Riemann-Sum Approximation is used to describe the flow behavior under combined magneto-electrohydrodynamic effects in time domain. Parametric results show that stronger magnetic fields damp velocity oscillations, while higher electrokinetic coupling enhances near-wall fluid motion due to EDL-induced slip. The interaction between magnetic field and electroosmotic forces determines the time required for full flow development. The findings provide insight into microscale transport in oil-brine mixtures and indicate that electrokinetic effects significantly increase both velocity and mass flow rate.

Key words: enhanced oil recovery, Riemann-Sum Approximation, electrokinetic effect, MHD; transient flow.

1. Introduction

With the reduction of the use of mechanical machines to create a carbon- free environment, the use of electro-kinetic effects continues to receive considerable attention, owing to their applications in medicine, engineering, and oil production. One of the most important applications of electro-kinetics is the design of defibrillators (A device used in cardiopulmonary resuscitation (CPR)) which delivers an electric current to the heart and is commonly used to treat ventricular fibrillation (VF) and non-perfusing ventricular tachycardia (VT) [1, 2]. In the field of civil engineering, the electro-kinetic effect has applications in the improvement of oil production and water purification. Anbah [3] demonstrated that the application of an external electric field to oil-water saturated media drives the electrophoretic transport of fluids toward the cathode. El-Sapa *et al.* [4] investigated the transient electrophoresis of conducting colloidal particles in porous media using a cell model and reported that increasing the permeability resistance parameter significantly reduces the flow rate and stream function while enhancing microrotation. The study also showed that zeta potential asymmetry can be used to control or even reverse the flow**.** Other relevant applications are found in soil engineering for soil drainage and electrochemical stabilization of soil [5]. Recent advances in electrokinetic phenomena have enabled the design of micropumps for applications in drug delivery, fuel transport, and biochemical reaction platforms [6]. Significant research has been conducted to characterize the flow development and heat transfer of electrokinetically driven fluids within cylindrical geometries [7-10].

The applications of electrically conductive fluid cannot be over-emphasised, ranging from power generation to the magneto-hydrodynamic (MHD) pump and the thermal recovery of oil. Gold [11] investigated the formation of MHD pipe flow and found that increasing magnetic field strength leads to decreasing flow rate. Later, Kumar and Rajathy [12] numerically carried out an investigation on MHD flow around a circular

* To whom correspondence should be addressed

cylinder at low to moderate Reynolds numbers. They concluded that the influence of Reynolds number is to increase flow rate. Sharma and Hemanta [13] studied the heat and mass transport in MHD flow generated by an axially moving cylinder, with radiation and thermal diffusion effects. All the above-mentioned literatures have considered only the steady-state problem. It is well known that for liquids with a low Reynolds number, the viscous forces are very strong relative to the inertia forces, and so the inertia forces have a smaller influence on the velocity field. The transitory state therefore has a negligible influence on the formation of flows. Ragab [14] examined transient electrophoresis of conducting colloidal particles in porous media using a cell model. The study derived closed-form expressions for electrophoretic velocity and provides analytical and numerical results describing the velocity behavior of conducting colloidal suspensions in porous environments, thereby extending previous steady and unsteady electrophoresis models. Also, Sherief *et al.* [15] investigated the transient electrophoretic motion of a conducting spherical particle in an electrolyte-saturated charged porous medium.

On the other hand, flow with high Reynolds number, the steady state analysis becomes insufficient to describe flow formation in any geometry. Singh and Lal [16] employed the finite difference approach to predict flow formation of MHD through pipes of various shapes, including rectangular, circular, and triangular sections. In other work, Boricic *et al.* [17] examined the MHD effect on unsteady dynamic flow within the boundary layer around a horizontal cylinder. Also, Deka and Paul [18] obtained an analytical solution for a turbulent free-flow MHD flow through an infinite cylinder and reported that the magnetic field slows the flow. Using the Laplace transform approach, several studies have investigated flow evolution and heat transfer in cylindrical geometries subjected to a transverse magnetic field [20-23].

Maurya *et al.* [24] developed an analytical solution describing the formation of transient magnetohydrodynamic flow within a circular cylinder. They employed the method of separation of variable and obtained the solution as an infinite series with computations of first fifty zeros of a first order modified Bessel function. These results demonstrate the attainment of steady state at large time intervals. The method is numerically rigorous; however, series convergence is typically achieved only at large time values, where the zeros of the first-order modified Bessel function are obtained by solving the corresponding transcendental equation.

The innovative element of this investigation lies in developing a transient semi-analytical formulation of magnetohydrodynamic flow coupled with electrokinetic effects in capillary-scale structures representative of porous oil reservoirs. The derived Bessel-type analytical solutions reveal the interplay between magnetic damping and electrokinetic acceleration mechanisms in determining transient flow formation in conductive hydrocarbon-brine systems. This coupling framework provides a theoretical foundation for subsurface electro-magnetically enhanced oil transport, offering predictive capability for designing field stimulation, smart drilling fluids, and EOR operations based on electrokinetic-MHD principles: a direction largely unexplored in current petroleum transport modelling literature.

The basic contributions in this article are as follow:

(a) The integration of electrokinetic effects allows for the precise regulation of mass flow rates.

(b) By optimizing control parameters, both skin friction and internal surface corrosion within the tube can be significantly minimized.

Major Advancements over Maurya *et al.* [24]

1. *Emergence of a Transition Regime*: The model identifies a distinct transition phase where the flow physics shifts from purely magnetohydrodynamic (MHD) dominance to a combined electrokinetic-MHD regime.
2. *Dual-Parameter Flow Control*: Unlike previous single-effect models, this framework introduces dual-parameter control, enabling the simultaneous optimization of fluid transport within capillary channels through both electrical and magnetic tuning.
3. *Synergistic Surface-Field Interactions:* Velocity and skin friction are found to be jointly regulated by electrical double layer (EDL) thickness and magnetic field strength. This interaction produces complex flow behaviours that are absent in models considering these effects in isolation.

4. *Altered Transient Development:* The introduction of electrokinetic forcing significantly modifies the transient evolution process, fundamentally changing the time scales required for the flow to reach a steady-state equilibrium.
5. *Dynamic Force Balancing*: The flow velocity is redefined as a precise balance between magnetic suppression and electrokinetic enhancement, allowing for more granular control over the velocity profile compared to traditional models.

1.1. Mathematical analysis

Consider an unsteady, laminar, fully developed flow of an electrically conducting fluid in a horizontal tube of radius $r_1^{'}$ in the presence of electrokinetic effect. The flow is propelled by a combination of external voltage gradient and constantly applied favourable pressure gradient in the direction of the flow. An electric potential ζ_1 is imposed on the tube's surface, as illustrated in Fig.1. The electric double layer (EDL) charge distribution obeys the Boltzmann distribution, thereby neglecting ionic convection effects. Moreover, the electric potential is assumed to be small enough to withstand Debye-Hückel linearization, which has been proven to be a reasonable approximation for describing the flow evolution in a tube (Liechty *et al.* [25]). The Debye-Hückel approximation is justified by the low concentration of dissociated ions and low dielectric constant of crude oil, ensuring the electrical double layer remains within the linear potential regime. Ionic convection on the other hand is neglected due to the high viscosity of the oil phase, which results in a low Péclet number ($Pe << 1$) where diffusive transport dominates over advection. The single-capillary representation provides a fundamental unit-cell model to isolate interfacial interactions from complex pore-scale tortuosity. Moreover, the applied external voltage is significantly larger than the flow-induced voltage. These assumptions remain valid for laminar flow in tight hydrocarbon reservoirs, though they may reach their limits in high-permeability zones or under significant pressure gradients.

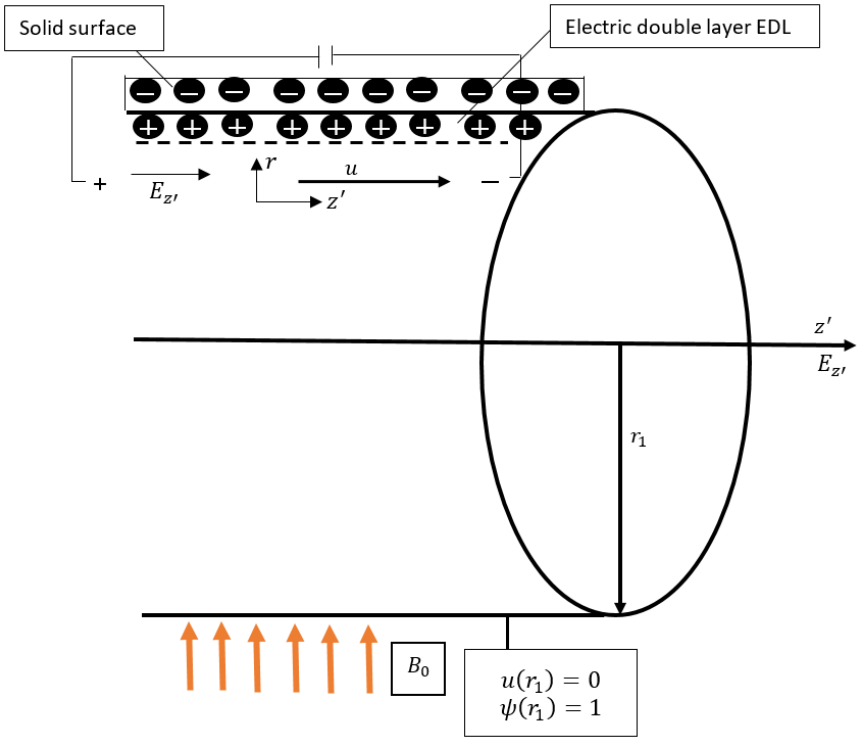

Fig.1. Schematic diagram of problem formulation.

Further, the externally applied voltage greatly exceeds the flow-induced voltage. Unless otherwise specified, all other thermophysical parameters are assumed to be constant.

2. Electric potential

Based on these assumptions, the electrical potential distribution is obtained by solving the Poisson-Boltzmann equation as follows:

$$\nabla^2\phi = -\frac{\rho_e}{\varepsilon}. \tag{2.1}$$

The combined effect of the external field Φ and the EDL-induced potential ψ', results in the potential ϕ. Where ρ_e is the net volume charge density of symmetric electrolyte and defined as [26]:

$$\rho_e = -2FZC_0 \sinh\left(\frac{ZF\psi'}{R'T}\right), \qquad \nabla = \frac{\partial}{\partial r}\vec{i} + \frac{1}{r}\frac{\partial}{\partial \phi}\vec{j} + \frac{\partial}{\partial z'}\vec{k}. \tag{2.2}$$

Since the flow is considered in a fully developed region, the external potential gradient exists solely in the axial direction, $\phi = \phi(r')$ and $\psi' = \psi'(r')$. Hence:

$$\left[\frac{1}{r'}\frac{\partial}{\partial r'}\left(r'\frac{\partial \psi'}{\partial r'}\right)\right] = \frac{2FZC_0}{\varepsilon}\sinh\left(\frac{ZF\psi'}{R'T}\right) \tag{2.3}$$

subject to the boundary conditions:

$$\frac{d\psi'(0)}{dr'} = 0, \qquad \psi'(r'_1) = \zeta_1 \tag{2.4}$$

where ζ_1 is the zeta-potential at the surface of the tube.
Applying the Debye-Hückel linearization, valid for small surface potentials, Eqs. (2.3) and (2.4) simplify to the following dimensionless forms:

$$\frac{d^2\psi}{dR^2} + \frac{1}{R}\frac{d\psi}{dR} - \kappa^2\psi = 0, \tag{2.5}$$

$$\frac{d\psi(0)}{dR} = 0, \qquad \psi(1) = 1, \tag{2.6}$$

where $$R = \frac{r'}{r_1}, \qquad \psi = \frac{\psi'}{\zeta_1}, \qquad \kappa = \frac{r_1}{\lambda_D}, \qquad \lambda_D = \left[\frac{\varepsilon R'T}{2F^2Z^2C_0}\right]^{1/2}. \tag{2.7}$$

Equation (2.5) is a Bessel's differential equation and the solution of Eqs. (2.5), considering boundary conditions (2.6), can be expressed as:

$$\psi = \frac{I_0(\kappa R)}{I_0(\kappa)}. \tag{2.8}$$

3. Flow field

Expanding the approach of Maurya *et al.* [24] to incorporate electrokinetic effects, the governing equations for the current physical system are defined as follows:

$$\rho\frac{\partial u'}{\partial t'} = G + \mu\left(\frac{\partial^2 u'}{\partial r'^2} + \frac{1}{r'}\frac{\partial u'}{\partial r'}\right) - \sigma B_0^2 u' - \varepsilon E_z\left[\frac{d^2\psi'}{dr'^2} + \frac{1}{r'}\frac{d\psi'}{dr'}\right]. \tag{3.1}$$

together with the following prescribed initial and boundary conditions:

$$t' \le 0,\quad u' = 0,\quad 0 \le r' \le 1,\qquad t' > 0\begin{cases} u' = \text{finite at } r' = 0, \\ u' = 0 \quad \text{at} \quad r' = r_1, \end{cases} \tag{3.2}$$

$$\begin{gathered} U = \frac{u'}{U_0},\quad Ha^2 = \frac{\sigma B_0^2 r_1^{\,2}}{\nu\rho},\quad t = \frac{Gt' r_1}{\mu},\quad A = -\frac{2\zeta_1 \mu F^2 Z^2 C_0}{r_1^{\,3}\rho G R' T U_0} E_z, \\ U_0 = \frac{Gr_1^2}{\mu},\quad Re = \frac{\rho U_0 r_1}{\mu},\quad Eu = \frac{Gr_1}{\rho U_0^{\,2}},\quad R = \frac{r'}{r_1}. \end{gathered} \tag{3.3}$$

Where the foregoing parameters are properly defined in the Appendix. The electrokinetic parameter (A) represents the dimensionless coupling between electrical potential and fluid flow, specifically quantifying the efficiency of electro-osmotic transport within the capillary. Physically, it scales the ability of the electrical double layer (EDL) to drive fluid motion under an applied field or to generate a streaming potential under a pressure gradient.

Employing the dimensionless variables introduced in Eq.(3.3), Eq.(3.1) and (3.2) reduce to:

$$\frac{\partial U}{\partial t} = Eu + \frac{1}{Re}\left(\frac{\partial^2 U}{\partial R^2} + \frac{1}{R}\frac{\partial U}{\partial R}\right) - \frac{Ha^2}{Re}U + A\psi(R). \tag{3.4}$$

And the initial and boundary conditions become:

$$t \le 0,\quad U = 0,\quad 0 \le R \le 1,\qquad t > 0\begin{cases} \dfrac{dU}{dR} = 0 \quad \text{at} \quad R = 0, \\ U = 0 \quad \text{at} \quad R = 1. \end{cases} \tag{3.5}$$

4. Steady state analysis

The solution at steady state for Eq.(3.4) with boundary conditions (3.5), is given by:

$$\left(\frac{d^2 U_s}{dR^2} + \frac{1}{R}\frac{dU_s}{dR}\right) - Ha^2 U_s = -Eu\,Re - ARe\frac{I_0(\kappa R)}{I_0(\kappa)}. \tag{4.1}$$

$$\frac{dU_s}{dR}=0 \quad \text{at} \quad R=0,$$
$$U_s=0 \quad \text{at} \quad R=1. \tag{4.2}$$

The solution to Eq.(4.1), satisfying the boundary conditions in Eq.(4.2), is given in closed form using the modified Bessel function of the first kind:

$$U_s=\frac{Eu\,Re}{Ha^2}\left[1-\frac{I_0(HaR)}{I_0(Ha)}\right]+\frac{ARe}{\left(\kappa^2-Ha^2\right)}\left[\frac{I_0(HaR)}{I_0(Ha)}-\frac{I_0(\kappa R)}{I_0(\kappa)}\right]. \tag{4.3}$$

5. Transient state analysis

Equation (3.4) is a second order non-homogeneous partial differential equation. It is convenient to transform it into homogeneous partial differential equation by defining a new velocity $U_z(R,t)$ using the following transformation:

$$U_z=U_s-U. \tag{5.1}$$

Substituting Eqs (5.1) into (3.4) and (3.5), the following second order homogeneous partial differential equation is obtained:

$$Re\frac{\partial U_z}{\partial t}=\left(\frac{\partial^2 U_z}{\partial R^2}+\frac{1}{R}\frac{\partial U_z}{\partial R}\right)-Ha^2U_z. \tag{5.2}$$

with the initial and boundary conditions:

$$t\le 0,\;\; U_z=U_s,\;\; 0\le R\le 1, \qquad t>0\begin{cases}\dfrac{dU_z}{dR}=0 \quad \text{at} \quad R=0,\\[2ex] U_z=0 \quad \text{at} \quad R=1.\end{cases} \tag{5.3}$$

Using the Laplace transform technique, defined as:

$$L\left[U(R,t)\right]=\bar{U}(R,S)=\int_0^\infty U(R,t)\exp(-St)\,dt, \qquad S>0. \tag{5.4}$$

Using Eq.(5.4), the partial differential Eq.(5.2) is transformed into ordinary differential equation:

$$\frac{d^2\bar{U}_z}{dR^2}+\frac{1}{R}\frac{d\bar{U}_z}{dR}-\left(Ha^2+ReS\right)\bar{U}_z=-\frac{EuRe}{S} \tag{5.5}$$

subject to

$$\frac{dU_z}{dR}=0 \text{ at } R=0, \quad \bar{U}_z=0 \text{ at } R=1. \tag{5.6}$$

The exact solution of Eq.(5.5) in Laplace domain with boundary condition (5.6) is:

$$\begin{aligned}\bar{U}_z(R,S)=&\frac{Eu\,Re}{Ha^2}\left[\frac{1}{Ha^2+ReS}-\frac{I_0(RHa)}{SReI_0(Ha)}\right]+\\&+\frac{ARe}{\left(\kappa^2-Ha^2\right)}\left[\frac{I_0(RHa)}{SReI_0(Ha)}-\frac{I_0(\kappa R)}{\left(\kappa^2-Ha^2-SRe\right)I_0(\kappa)}\right]+\\&+\frac{1}{S}\frac{I_0\left(R\sqrt{Ha^2+ReS}\right)}{I_0\left(\sqrt{Ha^2+ReS}\right)}\left[\frac{Eu}{Ha^2+ReS}+\frac{A}{\left(\kappa^2-Ha^2-SRe\right)}\right].\end{aligned} \tag{5.7}$$

The transient skin-friction at the tube inner surface and the mass flow rate are respectively given as:

$$\begin{aligned}\tau(R,S)=\left.\frac{d\bar{U}_z}{dR}\right|_{R=1}=&-\frac{Eu\,Re}{Ha}\frac{I_1(Ha)}{SReI_0(Ha)}+\\&+\frac{ARe}{\left(\kappa^2-Ha^2\right)}\left[\frac{HaI_1(Ha)}{SReI_0(Ha)}-\frac{\kappa I_1(\kappa)}{\left(\kappa^2-Ha^2-SRe\right)I_0(\kappa)}\right]+\\&+\frac{\sqrt{Ha^2+ReS}}{S}\frac{I_1\left(\sqrt{Ha^2+ReS}\right)}{I_0\left(\sqrt{Ha^2+ReS}\right)}\left[\frac{Eu}{Ha^2+ReS}+\frac{A}{\left(\kappa^2-Ha^2-SRe\right)}\right].\end{aligned} \tag{5.8}$$

$$\begin{aligned}Q(R,S)=\int_0^1 R\bar{U}_z(R,S)dR=&\frac{Eu\,Re}{Ha^2}\left[\frac{1}{2Ha^2+ReS}-\frac{I_1(Ha)}{HaSReI_0(Ha)}\right]+\\&+\frac{ARe}{\left(\kappa^2-Ha^2\right)}\left[\frac{I_1(Ha)}{HaSReI_0(Ha)}-\frac{I_1(\kappa)}{\kappa\left(\kappa^2-Ha^2-SRe\right)I_0(\kappa)}\right]+\\&+\frac{1}{S\sqrt{Ha^2+ReS}}\frac{I_1\left(\sqrt{Ha^2+ReS}\right)}{I_0\left(\sqrt{Ha^2+ReS}\right)}\left[\frac{Eu}{Ha^2+ReS}+\frac{A}{\left(\kappa^2-Ha^2-SRe\right)}\right].\end{aligned} \tag{5.9}$$

where I_0 and I_1 denote the modified Bessel functions of the first kind of orders zero and one, respectively, and are defined as follows:

$$I_0(R)=\sum_{k=0}^{\infty}\frac{\left(\frac{R^2}{4}\right)^k}{(k!)^2}, \qquad I_1(R)=\frac{R}{2}\sum_{k=0}^{\infty}\frac{\left(\frac{R^2}{4}\right)^k}{k!(k+1)!}. \tag{5.10}$$

6. Riemann-Sum Approximation (RSA)

Equations (5.7-5.9) yield solutions in the Laplace domain, which must be translated into the time domain. Due to the complex nature of the solutions in the Laplace domain, a numerical method was employed from [28-31] which relies on the Riemann-sum approximation (RSA). By applying this numerical technique, an arbitrary function in the Laplace domain can be transformed back into the time domain as follows:

$$U_z(R,t)=\frac{e^{\xi t}}{t}\left[\frac{1}{2}\bar{U}_z(R,\xi)+Real\sum_{n=1}^{M}\bar{U}_z\left(R,\xi+\frac{in\pi}{t}\right)(-1)^n\right],\quad 0\le R\le 1, \tag{6.1}$$

$$\tau_z(t)=\left.\frac{dU_z(R,t)}{dR}\right|_{R=1}=\frac{e^{\xi t}}{t}\left[\frac{1}{2}\frac{d\bar{U}_z(1,\xi)}{dR}+Real\sum_{n=1}^{M}\frac{d\bar{U}_z(1,\xi)}{dR}\left(1,\xi+\frac{in\pi}{t}\right)(-1)^n\right],\quad R=1, \tag{6.2}$$

$$Q_z(t)=\frac{e^{\xi t}}{t}\left[\frac{1}{2}Q(s)+Real\sum_{n=1}^{M}Q\left(\xi+\frac{in\pi}{t}\right)(-1)^n\right] \tag{6.3}$$

where Re is the real part and $i=\sqrt{-1}$ the imaginary number. M denotes the total number of terms used in the Riemann-sum approximation, and ξ denotes the real part of the Bromwich contour used for Laplace inversion. In this approach, Laplace inversion via the Riemann-sum approximation is carried out using a single summation over the whole numerical process. Its accuracy depends on the value of ε and the truncation error dictated by M. According to Tzou [32] and based on numerical inspection in the current analysis, the value of ξ that best satisfied the result is *4.7*. This inversion method has been shown to be an effective approach for converting any function from the Laplace domain to the time domain [28]. Equations (6.1-6.3) gives the time-dependent velocity, wall shear stress, and mass flow rate, respectively.
So that the overall velocity profile is given as:

$$U(R,t)=U_s(R)-U_z(R,t). \tag{6.4}$$

Similarly, the overall skin-friction and mass flowrate are given respectively as follow:

$$\tau=-\left.\frac{dU(R,t)}{dR}\right|_{R=1}=\left.\frac{dU_z(R,t)}{dR}\right|_{R=1}-\left.\frac{dU_s(R)}{dR}\right|_{R=1}, \tag{6.5}$$

$$Q=\int_0^1 RU_s(R)dR+\int_0^1 RU_z(R,S)dR\,. \tag{6.6}$$

7. Validation of result

To verify the reliability of the proposed model, the steady state (time independent) exact solution, obtained in Eq.(4.3) should match with the complicated solution of represented by Eq.(6.4) at large time. As presented in Tab.1, an excellent agreement is found for these numerical comparisons at large time. The steady solution is independent of time (t) and therefore does not change with time from Tab.1.

8. Special cases

8.1. Absence of magnetic field (*Ha=0*)

In the absence of uniformly applied magnetic field, the governing Eq.(3.4) reduces to:

$$\frac{\partial U_1}{\partial t} = Eu + \frac{1}{Re}\left(\frac{\partial^2 U_1}{\partial R^2} + \frac{1}{R}\frac{\partial U_1}{\partial R}\right) + ARe\frac{I_0(\kappa R)}{I_0(\kappa)}. \tag{8.1}$$

with the initial and boundary conditions:

$$\begin{aligned} &t \le 0,\ U_1 = 0,\ \ 0 \le R \le 1, \\ &t > 0 \begin{cases} U_1 = \text{finite} \quad \text{at} \quad R = 0, \\ \\ U_1 = 0 \quad \text{at} \quad R = 1. \end{cases} \end{aligned} \tag{8.2}$$

The solution of Eq.(8.1) subject to (8.2) is given as:

$$U_1 = \frac{Eu}{4}\left(1 - R^2\right) + \frac{A}{\kappa^2}\left[1 - \frac{I_0(\kappa R)}{I_0(\kappa)}\right] - U_2(R,t)$$

where
$$U_2(R,t) = \frac{e^{\varepsilon t}}{t}\left[\frac{1}{2}\bar{U}_2(R,\varepsilon) + Re\sum_{n=1}^{M}\bar{U}_2\left(R,\varepsilon + \frac{in\pi}{t}\right)(-1)^n\right], \quad 0 \le R \le 1 \tag{8.3}$$

and
$$\begin{aligned} \bar{U}_2(R,S) = &\frac{EuI_0\left(R\sqrt{ReS}\right)}{I_0\left(\sqrt{ReS}\right)}\left[\frac{1}{Re^2S^2} - \frac{A}{ReS\left(\kappa^2 - ReS\right)}\right] - \\ &+ \frac{Eu}{4}\left[\frac{R^2}{ReS} + \frac{4}{Re^2S^2}\right] + \frac{A}{\kappa^2}\left[\frac{1}{ReS} + \frac{I_0(\kappa R)}{\left(\kappa^2 - ReS\right)I_0(\kappa)}\right]. \end{aligned} \tag{8.4}$$

8.2. Absence of electrokinetic effect (*A=0*)

In the absence of the electrokinetic effect, the current physical scenario aligns exactly with the results reported by Maurya *et al.* [24]. This study employs a more efficient mathematical approach for solving partial differential equations, offering a promising and simpler alternative to the complex method used in [24]. For validation, Tab.2 provides a numerical comparison of the velocity profiles between the two studies with the electrokinetic effect omitted, showing excellent agreement. Furthermore, the calculated percentage change demonstrates that the presence of the electrokinetic effect significantly enhances flow formation.

8.3. Results and discussion

This study analyzes the influence of electrokinetic effects on transient flow within a horizontal tube under an external transverse magnetic field. Given its relevance to subsurface oil transport, the governing

parameters are aligned with those of Maurya *et al.* [24] to validate the accuracy of the current findings. The basic parameter controlling the flow formation are the Hartmann number (Ha) which represents the magnitude of applied magnetic field, the Debye-Huckel parameter (κ) which is inversely proportional to the EDL length, the Euler number (Eu), the Reynolds number (Re) and the dimensionless parameter responsible for electrokinetic effect (A). The following numerical values are used to justify the physics of the flow, $0.5 \le Ha \le 5$, $0.5 \le \kappa \le 50$, $0 \le Eu \le 1$, $0 \le Re \le 20$, $0 \le A \le 2$.

Table 1. A numerical comparison between the transient velocity profile and the corresponding steady-state solution for $Re = 10,\ Ha = 2.0,\ Eu = 0.8,\ A = 2.0$.

		Transient state	Steady state
R	t	$U(R,t)$	$U(R)$
0	0.1	0.057108	1.084479
	1	0.561012	1.084479
	5	1.073710	1.084479
	SS	1.084479	1.084479
0.2	0.5	0.059284	1.069902
	1	0.572767	1.069902
	5	1.059746	1.069902
	SS	1.069902	1.069902
0.5	0.5	0.075814	0.969683
	1	0.605899	0.969683
	5	0.962468	0.969683
	SS	0.969683	0.969683
0.8	0.5	0.125178	0.626379
	1	0.476568	0.626379
	5	0.623493	0.626379
	SS	0.626379	0.626379

Table 2. A numerical comparison of the velocity from the present study with that reported by Maurya *et al.* [24] at various times for $Re = 10,\ Ha = 2.0,\ Eu = 0.8,\ R = 0$.

		Present $U(R,t)$		
t	Maurya *et al.* [24]	$A = 0$	$A = 2$	% change
0	0.0000214588292	0.000614386737	0.0007490224	21.914
1	0.6379930032805	0.6379986143141	0.8002610986	25.433
10	1.1225735580113	1.1225735680210	1.5053630509	34.099
20	1.1226474361590	1.1226474361602	1.5054716128	34.100
30	1.1226474403257	1.1226474403257	1.5054716189	34.100
35	1.1226474403259	1.1226474403259	1.5054716189	34.100
40	1.1226474403259	1.1226474403259	1.5054716189	34.100
45	1.1226474403259	1.1226474403259	1.5054716189	34.100
50	1.1226474403259	1.1226474403259	1.5054716189	34.100
55	1.1226474403259	1.1226474403259	1.5054716189	34.100
60	1.1226474403259	1.1226474403259	1.5054716189	34.100
65	1.1226474403259	1.1226474403259	1.5054716189	34.100

9. Sensitivity analysis

The sensitivity index (S_χ) for each parameter χ was determined by examining the percentage change in the selected response variable skin-friction resulting from a small perturbation $(\pm 10\%)$ in the parameter value. The normalized sensitivity index is expressed as [33]:

$$S_\chi = \frac{S_{A_i}}{\sum S_{A_i}} \times 100 \tag{9.1}$$

where χ are parameters of interest, $\Delta\chi = 10\%$ of χ,

$$S_{A_I} = \frac{\tau_0(\chi+\Delta\chi) - \tau_0(\chi-\Delta\chi)}{(\chi+\Delta\chi)-(\chi-\Delta\chi)} \ . \tag{9.2}$$

It is clear from Tab.3 and Fig.13 that κ and Ha have reducing effect on skin-friction, while A, Eu, t, Re have increasing tendency.

9.1. Velocity profile

Figure 2 illustrates the competing influences of the Hartmann number (Ha) and the electrokinetic parameter (A) on the transient velocity profile. The results indicate that fluid velocity is enhanced by increasing but suppressed by increasing Ha. Physically, a higher value of A strengthens the dimensionless electric potential gradient, which amplifies the longitudinal electrostatic force acting on the species, thereby accelerating the flow. Conversely, an increase in Ha signifies a dominant Lorentz force, which acts in opposition to the flow direction, providing a magnetic damping effect that reduces fluid velocity. These dynamics are critical for optimizing flow-rate control in subsurface oil recovery.

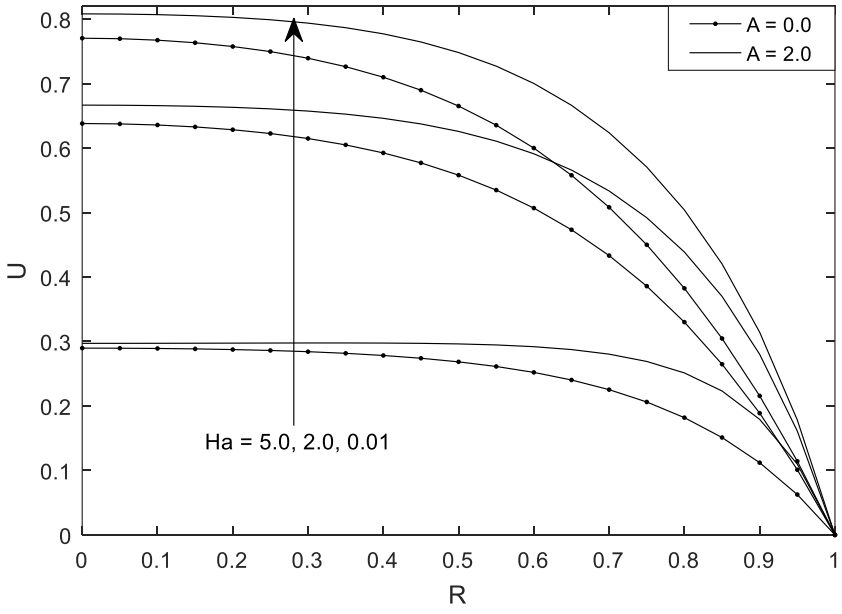

Fig.2. Velocity profile for different values of A and Ha for $t = 1.0,\ Re = 10.0,\ Eu = 0.8,\ \kappa = 10.0$.

Figure 3 illustrates the synergistic impact of the Euler number (Eu) and the electrokinetic parameter (A) on the velocity profile. The results indicate that the fluid velocity is directly proportional to both parameters, reflecting a state where two distinct driving mechanisms act in unison. The Euler number represents the ratio of pressure forces to inertial forces. Physically, an increase in Eu corresponds to a higher longitudinal pressure gradient across the horizontal tube. This gradient acts as the primary mechanical driver, imparting linear momentum to the bulk fluid and overcoming the viscous resistance at the tube walls. Simultaneously, the electrokinetic parameter (A) enhances the Coulombic body force within the Electric Double Layer (EDL).

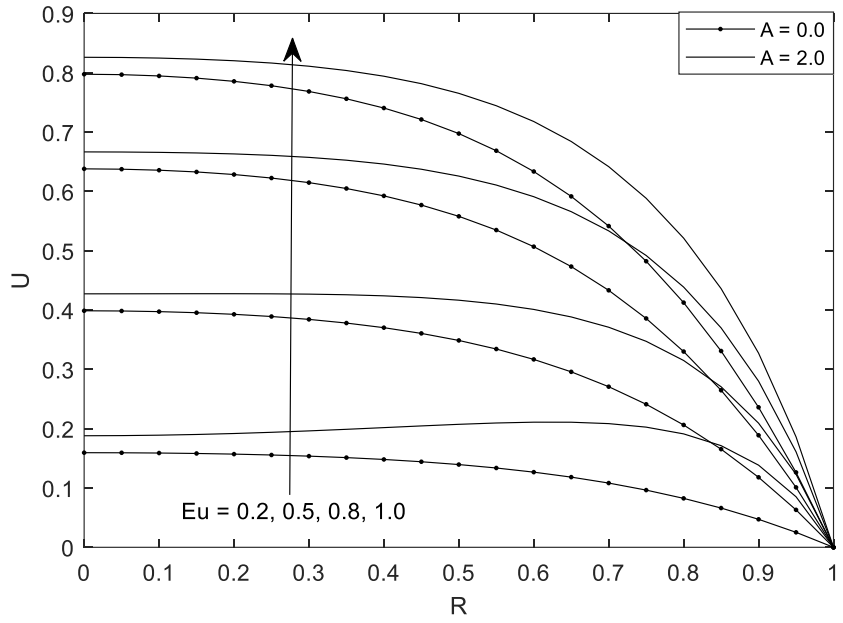

Fig.3. Velocity profile for different values of A and Eu at $Ha = 2.0,\ Re = 10.0,\ t = 1.0,\ \kappa = 10.0$.

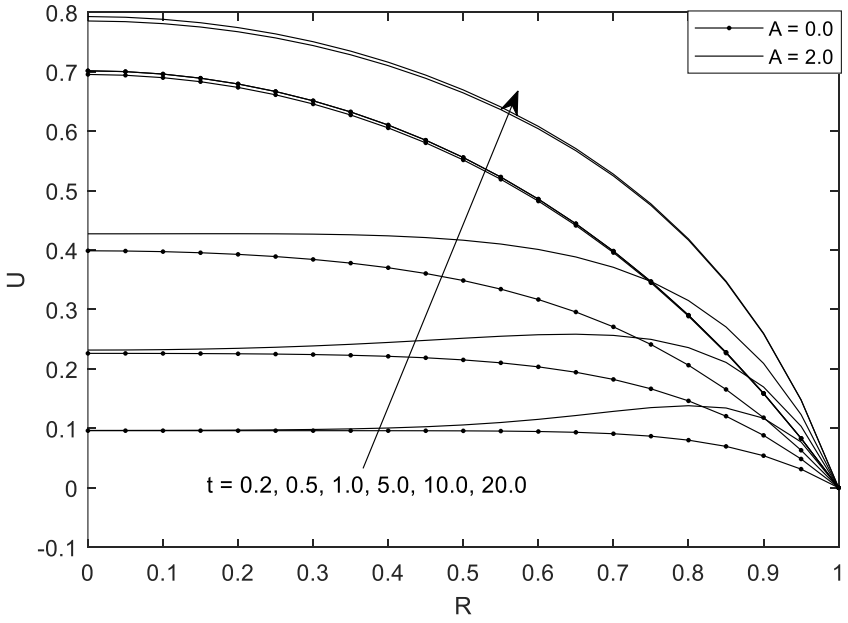

Fig.4. Velocity profile for different values of A and t at $Ha = 2.0,\ Re = 10.0, Eu = 0.5,\ \kappa = 10.0$.

When an external electric field is applied, it exerts a force on the net charge density near the wall. Because the pressure gradient and the electrokinetic force are aligned in the same direction, they create a constructive superposition of forces. In the context of subsurface oil transport, this demonstrates that the flow can be significantly accelerated by coupling mechanical pumping (high Eu) with electrokinetic stimulation (high A). This dual-driving mechanism is particularly effective in overcoming the viscous drag and magnetic damping inherent in complex geological formations. Figure 4 demonstrates the impact of electrokinetic effect on fluid velocity at different time. The velocity is observed to increase with time, irrespective of whether the electrokinetic effect is present or absent. It can be concluded from this figure that the role of magnitude of electrokinetic effect is to increase fluid velocity.

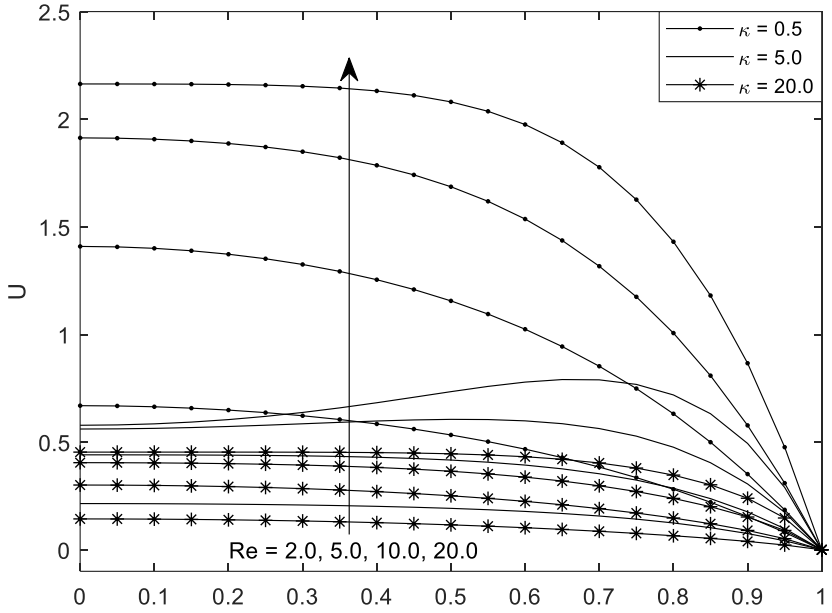

Fig.5. Velocity profile for different values of κ and Re at $Ha = 2.0, t = 1.0, Eu = 0.5, A = 2.0$.

Figure 5 on the other hand displays variation of fluid velocity with Reynolds number and Debye-Huckel parameter (κ). It is observed from this figure that fluid velocity is directly proportional to Re while the converse is true with κ. This occurs because a higher Reynolds number (Re) strengthens the viscous force in the direction of the favorable pressure gradient, promoting flow development. A closer examination of the figure also shows that the velocity gradient gradually diminishes as Re increases. Conversely, the maximum fluid velocity is observed at low values of κ, which corresponds to a thicker electric double layer (EDL). This is attributed to the fact that a larger EDL raises the surface electric potential, thereby enhancing the fluid's kinematic motion.

Table 3. Sensitivity analysis $S(\chi)$ of key dimensionless parameters for Skin-friction 10% change.

χ	χ	$\chi+\Delta\chi$	$\chi-\Delta\chi$	$\tau(\chi+\Delta\chi)$	$\tau(\chi-\Delta\chi)$	SA_I	$S(\chi)$ (%)
A	*2*	*2*	*1.8*	*4.7553*	*4.2321*	*2.62*	*39.48*
κ	*5*	*5.5*	*4.5*	*4.3366*	*4.6721*	*-0.34*	*-5.06*
Eu	*0.5*	*0.55*	*0.45*	*4.6815*	*4.3059*	*3.76*	*56.68*
t	*1*	*1.1*	*0.9*	*4.538*	*4.4372*	*0.50*	*7.61*
Ha	*2*	*2.2*	*1.8*	*4.4289*	*4.5545*	*-0.31*	*-4.74*
Re	*10*	*11*	*9*	*4.8872*	*4.088*	*0.40*	*6.03*

9.2. Skin-friction

Figures 6-9 display the transient skin-friction at the inner surface of the horizontal tube for different controlling parameters. This analysis is significant as it can help in optimising the occurrence of rusting or corrosion.

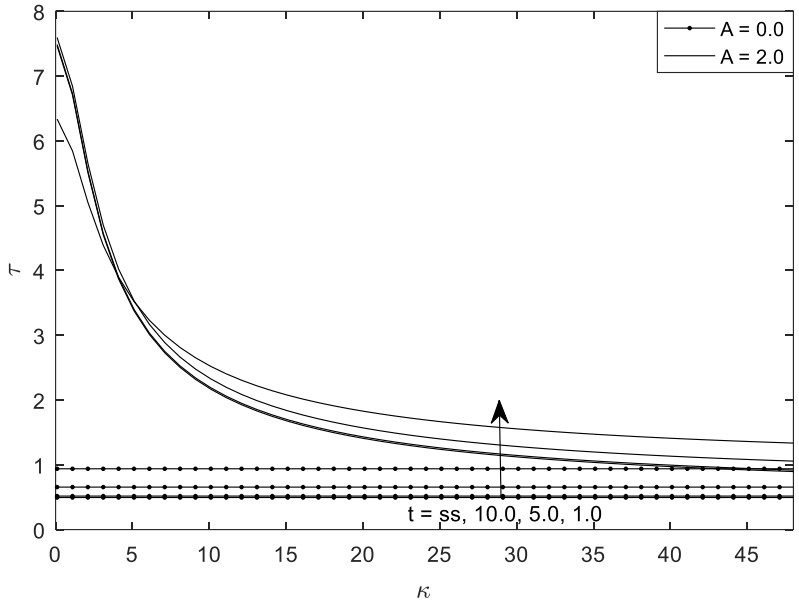

Fig.6. Skin-friction at different time for different values A at $Ha = 2.0$, $Eu = 0.8$, $Re = 10.0$.

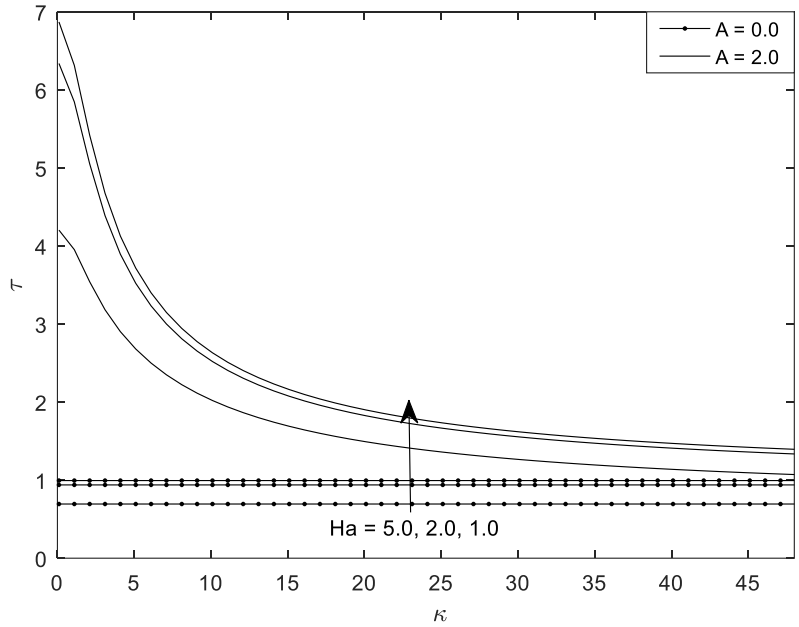

Fig.7. Skin-friction for different values of A at Ha at $t = 1.0$, $Eu = 0.5$, $Re = 10.0$.

Figure 6 depicts the skin-friction for various values of κ at different time instances. It is interesting to note that for thin EDL $(\text{large values of } \kappa)$, skin-friction decreases with increase in time as well as κ until

steady-state is attained regardless of the presence or absence of A while the reverse is true for large EDL $(\text{small values of } \kappa)$. A close examination of this figure reveals that as $\kappa \to \infty$, the skin friction becomes independent of the electrokinetic parameter (A). Physically, this occurs because an infinitely large Debye-Hückel parameter corresponds to a vanishingly thin Electric Double Layer (EDL). As the EDL thickness approaches zero, the electrokinetic body force is confined to a negligible region near the wall, effectively neutralizing its influence on the bulk flow and the resulting shear stress.

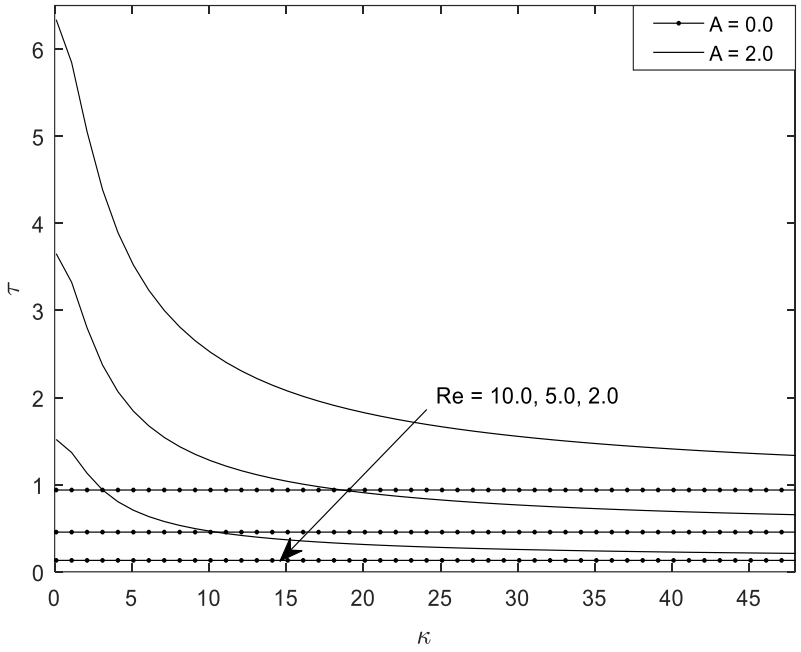

Fig.8. Skin-friction for different values of A at Re at $t = 1.0$, $Eu = 0.5$, $Ha = 2.0$.

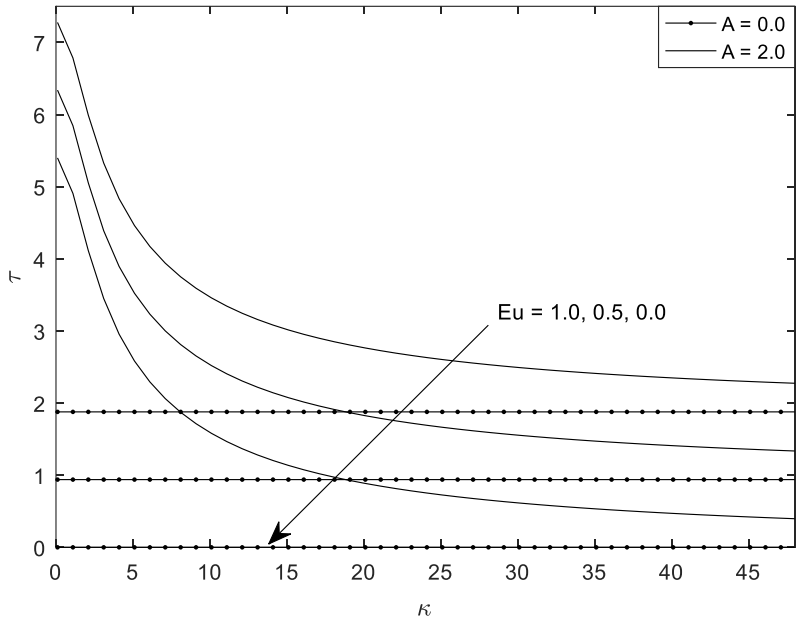

Fig.9. Skin-friction for different values of A at Eu at $t = 1.0$, $Re = 10.0$, $Ha = 2.0$.

Figure 7 on the other hand displays the role of Ha and A on skin-friction for different EDL length. It is found that skin-friction decreases with increase in Ha and κ. In addition, it can be deduced that the removal of electrokinetic effect leads to a corresponding reduction in skin-friction at the inner surface of the tube in transient state.

Figure 8 depicts the skin-friction as a function of the Reynolds number (Re) for various values of A, and different EDL thicknesses. The graph clearly shows that skin-friction rises with increasing Re. This trend can be explained by the fact that a higher Re results in an increased favourable pressure gradient, which boosts fluid velocity and, consequently, elevates the velocity gradient near the tube surface.

Figure 9 illustrates the role of Euler number (Eu) on transient skin-friction for different values of κ. It is established that skin-friction is an increasing function of Eu Independently of the EDL thickness. A critical look at Figures 6-9 clarifies that skin-friction is free from electro kinetic effect for very thin EDL $(\kappa \to \infty)$.

9.3. Mass flowrate

Another expression of engineering interest is the mass flowrate, which accounts for the amount of fluid passing through the horizontal tube at a given time. This analysis is significant as the obtained results can help to optimise flowrate of fluid at micro scale level. Figures 10-12 portray the role of various controlling parameters on mass flowrate in the horizontal tube at transient state.

Figure 10 represents the mass flowrate in the horizontal tube for dissimilar values of A and different EDL thickness at different time. The mass flowrate is seen to increase with time until steady state regardless of the EDL size or magnitude of electrokinetic effect. Also, a higher flowrate is achieved in presence of electro kinetic effect. This result suggests that the electrokinetic effect should not be neglected in improving oil exploration and flow formation.

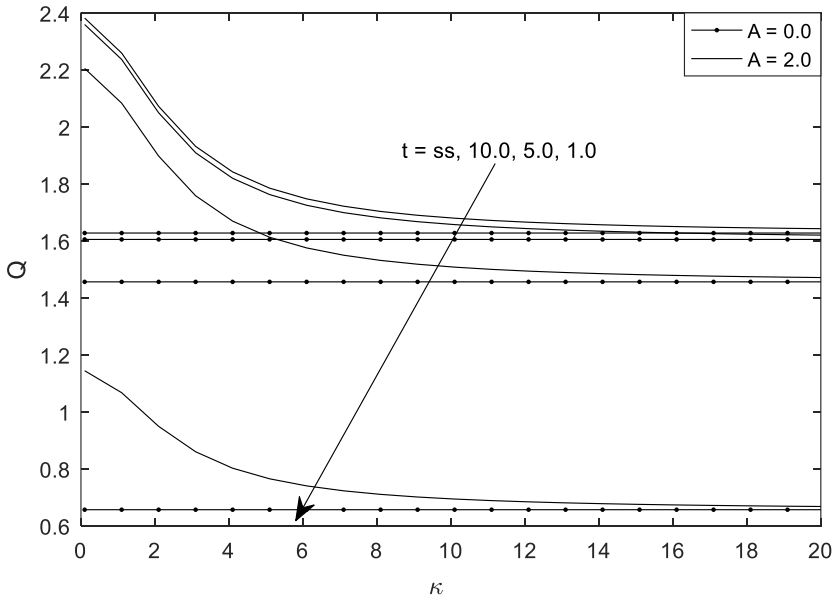

Fig.10. Mass flowrate for different values of A and t at $Eu = 0.5$, $Re = 10.0$, $Ha = 2.0$.

Similar investigation to Fig.10 is carried out in Figs 11 and 12 where mass flowrate is varied with Hartmann number (Ha) and Euler number (Eu) respectively. It is found from Fig.11 that mass flowrate is a decreasing function of Ha. This could be attributed to the presence of Lorenz force which retards fluid velocity and thereby reducing mass flowrate. Likewise, mass flowrate is found to increase with increase in Eu in the

horizontal circular tube regardless of the EDL thickness as shown in Fig.12. Further, in the absence of pressure gradient and electrokinetic effect $\left(Eu=0, A=0\right)$, mass flowrate is seen to be zero, regardless of the EDL size. A close inspection of Figs 10-12 reveals that flow behavior becomes independent of the electrokinetic effect as $\kappa \to \infty$, a result that aligns with the findings of Maurya *et al.* [24]. Physically, this occurs because an infinitely large Debye-Hückel parameter corresponds to a vanishingly thin Electric Double Layer (EDL). As the EDL thickness approaches zero, the electrokinetic body force is confined to a negligible region near the wall, effectively neutralizing its influence on the bulk flow and making the system purely hydrodynamic.

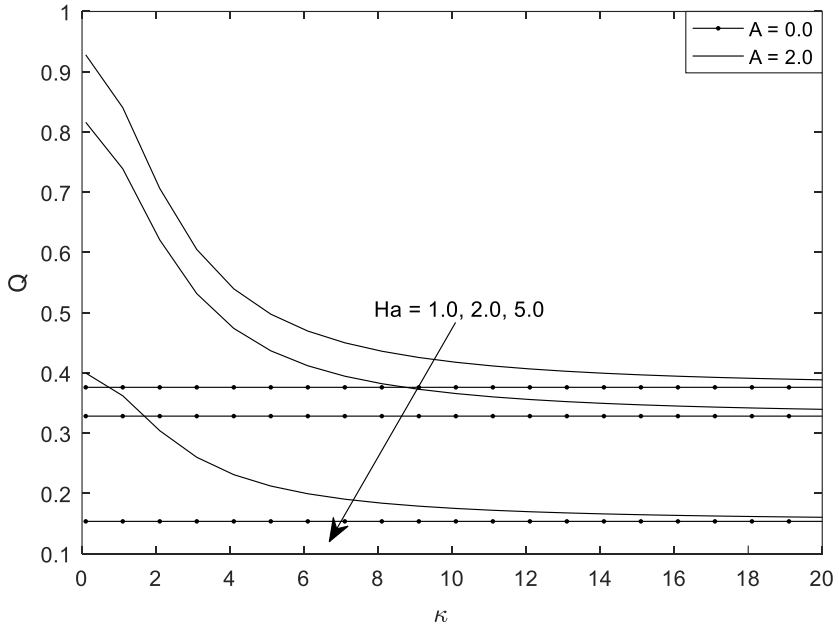

Fig.11. Mass flowrate for different values of A and Ha at $Eu=0.5, Re=10.0, t=1.0$.

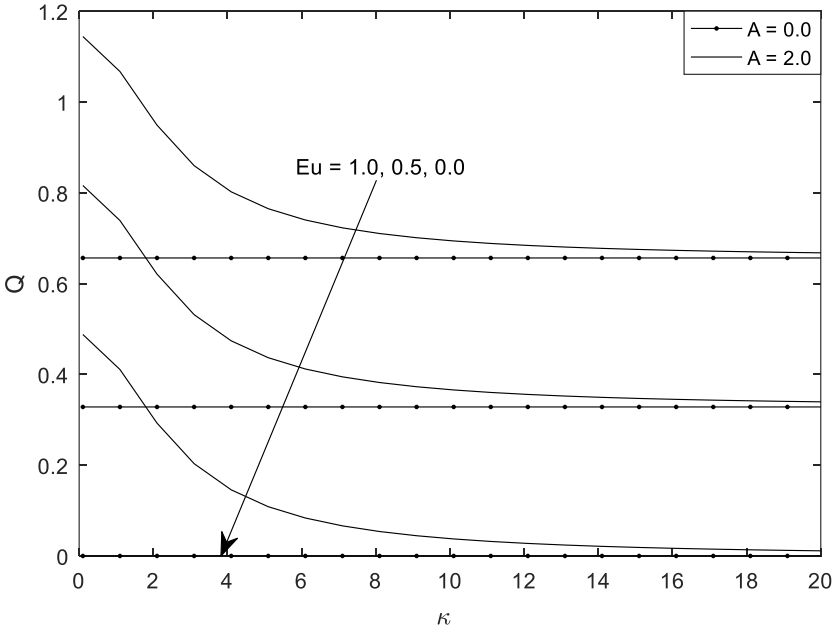

Fig.12. Mass flowrate for different values of A and Eu at $t=1.0, Re=10.0, Ha=2.0$.

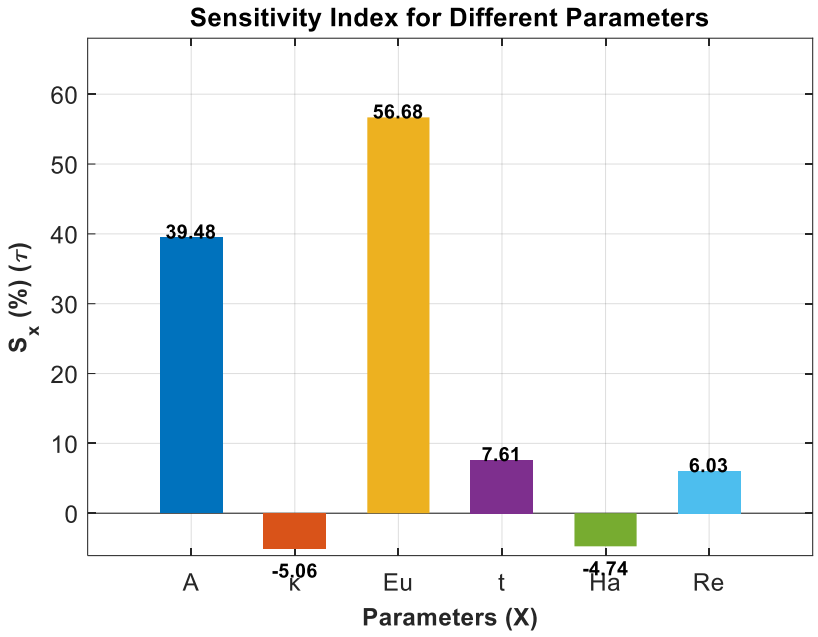

Fig.13. Sensitivity indices for skin-friction at the wall $Y=0$.

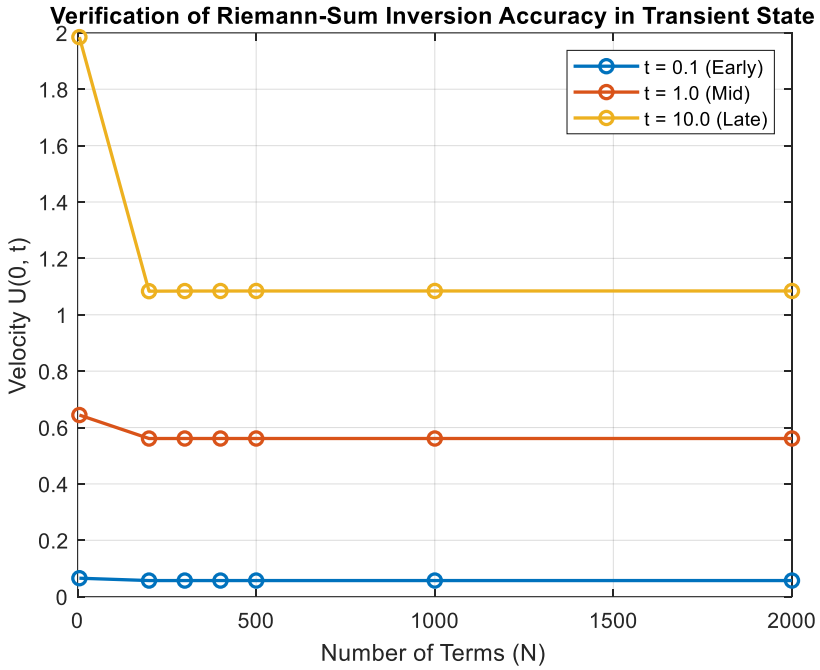

Fig.14. Verification of RSA inversion accuracy at different transient state.

To ensure the accuracy of the transient solution, the convergence of the Riemann-Sum inversion was tested by monitoring the velocity response at various non-steady-state time intervals is shown in Fig.14. As the number of terms in the summation (N) increases, the solution asymptotically approaches a constant value, with numerical residues dropping below a tolerance of 10^{-5} for $N \geq 100$. The use of RSA method provides a robust

inversion that is independent of the sampling frequency, confirming that the calculated transient behavior is a true representation of the governing equation rather than a numerical artifact.

10. Conclusion

The present study formulates a semi-analytical framework to analyze transient magnetohydrodynamic (MHD) flow with electrokinetic effects in a cylindrical capillary channel. In contrast to earlier investigations that treated MHD flow and electroosmotic flow independently, this work considers their combined influence. The interaction between the Lorentz force and the electric double layer (EDL) induced electroosmotic force, which is therefore incorporated into the unified model. Furthermore, the model establishes a two-parameter control strategy based on the Hartmann number and the Debye-Hückel parameter, which provides a practical means to regulate velocity distribution, wall shear (skin friction), and volumetric flow rate in microscale transport systems. The following conclusions are drawn from the entire simulation:

1. Fluid velocity, skin-friction and mass flowrate increases with increase in electro kinetic effect.
2. Skin-friction for thick EDL differs conversely from those of thin EDL at the tube surface.
3. Skin-friction and mass flowrate are independent of electro-kinetic effect for thin EDL.
4. Flow formation can be optimized by selecting suitable value for various controlling parameters.

11. Data availability section

No data was used. Matlab programmed codes may be made available from the corresponding author upon reasonable request.

Nomenclature

A – dimensionless zeta-potential parameter
c_0 – concentration of ions in bulk fluid
B_0 – magnetic field strength
Eu – Euler number
$E_{z'}$ – electrostatic intensity
F – Faraday's constant
G – negative applied pressure gradient $\left(-\partial p / \partial z'\right)$
g – acceleration due to gravity
Q – mass flow-rate
Ha – Hartmann number
p – pressure
R – dimensionless radial coordinate
Re – Reynolds number
R' – universal gas constant
r'_1 – radius of the cylinder
r' – dimensional radial coordinate
T – temperature of the fluid
t – dimensionless time
t' – dimensional time
U – dimensionless velocity
U_0 – characteristic velocity

u' – dimensional velocity

Z – valence number of ions in the solution

z' – axial coordinate

ε – fluid permittivity

ζ_1 – zeta – potential (electrokinetic potential of the wall in the double layer)

κ – Debye-Huckel parameter

λ_D – Debye length

μ – fluid dynamic viscosity

ν – kinematic viscosity

ρ – fluid density

ρ_e – charge density

σ – electrical conductivity of the fluid

τ – skin-friction

Φ – externally imposed electrostatic potential

ϕ – electrostatic potential

ψ – dimensionless EDL potential

ψ' – dimensional EDL potential

References

[1] Ong M.E, Lim S. and Venkataraman A. (2016): *Defibrillation and Cardioversion*.– In: Tintinalli J.E., Stapczynski J.S., Ma O.J., Yealy D.M., Meckler G.D. and Cline D.M. (Eds.), Tintinalli's Emergency Medicine: A Comprehensive Study Guide, 8th Ed., McGraw-Hill, New York.

[2] Kerber R.E. (2011): *Indications and techniques of electrical defibrillation and cardioversion*.– Hurst's The Heart, vol.1, pp.1088-1093.

[3] Anbah S.A., Chilingar G.V. and Beeson C.M. (1965): *Application of electrokinetic phenomena in civil engineering and petroleum engineering*.– Annals of the New York Academy of Sciences, vol.118, No.14, pp.587-602, https://doi.org/10.1111/j.1749-6632.1965.tb40730.x.

[4] El-Sapa S., Faltas M.S. and Ragab K.E. (2025): *Oscillatory Brinkman-micropolar electroosmosis in cylindrical microannuli*.– Chinese Journal of Physics, vol.97, pp.1464-1491, https://doi.org/10.1016/j.cjph.2024.12.015.

[5] Karniadakis G., Beskok A. and Aluru N. (2005): *Microflows and Nanoflows: Fundamentals and Simulation*.– Springer New York, https://doi.org/10.1007/b138244.

[6] Jha B.K. and Oni M.O. (2018): *Fully developed mixed convection flow in a vertical channel with electrokinetic effects: exact solution*.– Multidiscipline Modeling in Materials and Structures, vol.14, No.5, pp.1031-1041, https://doi.org/10.1108/MMMS-12-2017-0158.

[7] Chakraborty S. and Ray S. (2008): *Mass flow-rate control through time periodic electro-osmotic flows in circular microchannels*.– Physics of Fluids, vol.20, No.8, 083602, https://doi.org/10.1063/1.2969348.

[8] Kirby B.J. and Hasselbrink Jr E.F. (2004): *Zeta potential of microfluidic substrates: 2. Data for polymers*.– Electrophoresis, vol.25, No.2, pp.203-213, https://doi.org/10.1002/elps.200305755.

[9] Wang C.Y., Liu Y.H. and Chang C.C. (2008): *Analytical solution of electro-osmotic flow in a semicircular microchannel*.– Physics of Fluids, vol.20, No.6, 063105, https://doi.org/10.1063/1.2946445.

[10] Jian Y., Yang L. and Liu Q. (2010): *Time periodic electro-osmotic flow through a microannulus*.– Physics of Fluids, vol.22, No.4, 042001, https://doi.org/10.1063/1.3358473.

[11] Gold R.R. (1962): *Magnetohydrodynamic pipe flow. Part 1*.– Journal of Fluid Mechanics, vol.13, No.4, pp.505-512, https://doi.org/10.1017/S002211206200086X.

[12] Kumar H. and Rajathy R. (2006): *Numerical study of MHD flow past a circular cylinder at low and moderate Reynolds numbers*.– International Journal for Computational Methods in Engineering Science and Mechanics, vol.7, No.6, pp.461-473, https://doi.org/10.1080/15502280600936666.

[13] Sharma B.R. and Konwar H. (2015): *MHD flow, heat and mass transfer due to axially moving cylinder in presence of thermal diffusion, radiation and chemical reactions in a binary fluid mixture*.– International Journal of Computer Applications, vol.110, No.15, pp.30-38, https://doi.org/10.5120/19385-1100.

[14] Ragab K.E. (2023): *An investigation of the transient electrophoresis of conducting colloidal particles in porous media using a cell model*.– Chinese Journal of Physics, vol.85, pp.326-344, https://doi.org/10.1016/j.cjph.2023.06.012.

[15] Sherief H.H., Faltas M.S. and Ragab K.E. (2021): *Transient electrophoresis of a conducting spherical particle embedded in an electrolyte-saturated Brinkman medium*.– Electrophoresis, vol.42, No.16, pp.1636-1647, https://doi.org/10.1002/elps.202100067.

[16] Singh B. and Lal J. (1984): *Finite element method for unsteady MHD flow through pipes with arbitrary wall conductivity*.– International Journal for Numerical Methods in Fluids, vol.4, No.3, pp.291-302, https://doi.org/10.1002/fld.1650040308.

[17] Boričić A.Z., Jovanović M.M. and Boričić B.Z. (2012): *MHD effects on unsteady dynamic, thermal and diffusion boundary layer flow over a horizontal circular cylinder*.– Thermal Science, vol.16, No. suppl. 2, pp.311-321, https://doi.org/10.2298/TSCI120516147B.

[18] Deka R.K. and Paul A. (2013): *Transient free convective MHD flow past an infinite vertical cylinder*.– Theoretical and Applied Mechanics, vol.40, No.3, pp.385-402, https://doi.org/10.2298/TAM1303385D.

[19] Jha B.K. and Oni M.O. (2018): *Transient natural convection flow between vertical concentric cylinders heated/cooled asymmetrically*.– Proceedings of the Institution of Mechanical Engineers, Part A: Journal of Power and Energy, vol.232, No.7, pp.926-939, https://doi.org/10.1177/0957650918758743.

[20] Jha B.K. and Apere C.A. (2010): *Unsteady MHD Couette flows in an annuli: the Riemann-sum approximation approach*.– Journal of the Physical Society of Japan, vol.79, No.12, 124403, https://doi.org/10.1143/JPSJ.79.124403.

[21] Jha B.K. and Oni M.O. (2018): *Electromagnetic natural convection flow in a vertical microchannel with Joule heating: exact solution*.– Journal of Taibah University for Science, vol.12, No.5, pp.661-668, https://doi.org/10.1080/16583655.2018.1511252.

[22] Lutera J.N., Shekar M.R. and Goud B.S. (2025): *Numerical method of radiation impact on unsteady MHD nanofluid flow past an accelerated vertical porous plate with heat source*.– International Journal of Modelling and Simulation, vol.45, No.6, pp.2216-2224, https://doi.org/10.1080/02286203.2024.2384732.

[23] Oni M.O., Adebayo S.Y., Yusuf T.S. and Jha B.K. (2026): *Coupled electroosmotic-electromagnetohydrodynamic transport in a vertical microchannel with suction/injection: Heat and mass transfer analysis for Lab-on-a-Chip cooling applications*.– Propulsion and Power Research, [in Press], https://doi.org/10.1016/j.jppr.2024.11.001.

[24] Maurya J.P., Yadav S.L. and Singh A.K. (2018): *Magnetohydrodynamic transient flow in a circular cylinder*.– International Journal of Dynamics and Control, vol.6, No.4, pp.1477-1483, https://doi.org/10.1007/s40435-018-0406-2.

[25] Liechty B.C., Webb B.W. and Maynes R.D. (2005): *Convective heat transfer characteristics of electro-osmotically generated flow in microtubes at high wall potential*.– International Journal of Heat and Mass Transfer, vol.48, No.12, pp.2360-2371, https://doi.org/10.1016/j.ijheatmasstransfer.2005.01.002.

[26] Chang L., Jian Y., Buren M., Liu Q. and Sun Y. (2016): *Electroosmotic flow through a microtube with sinusoidal roughness*.– Journal of Molecular Liquids, vol.220, pp.258-264, https://doi.org/10.1016/j.molliq.2016.04.103.

[27] Rojas G., Arcos J., Peralta M., Méndez F. and Bautista O. (2017): *Pulsatile electroosmotic flow in a microcapillary with the slip boundary condition*.– Colloids and Surfaces A: Physicochemical and Engineering Aspects, vol.513, pp.57-65, https://doi.org/10.1016/j.colsurfa.2016.10.053.

[28] Jha B.K. and Oni M.O. (2018): *An analytical solution for temperature field around a cylindrical surface subjected to a time dependent heat flux: an alternative approach*.– Alexandria Engineering Journal, vol.57, No.2, pp.927-929, https://doi.org/10.1016/j.aej.2017.01.003.

[29] Khadrawi A.F. and Al-Nimr M.A. (2007): *Unsteady natural convection fluid flow in a vertical microchannel under the effect of the dual-phase-lag heat-conduction model*.– International Journal of Thermophysics, vol.28, No.4, pp.1387-1400, https://doi.org/10.1007/s10765-007-0245-5.

[30] Oni M.O. and Jha B.K. (2020): *Electroosmotic natural convection flow in a vertical microchannel with asymmetric heat fluxes*.– SN Applied Sciences, vol.2, No.10, 1638, https://doi.org/10.1007/s42452-020-03437-0.

[31] Rilwan U.S., Oni M.O., Jibril H.M. and Jha B.K. (2023): *Effects of Joule heating and viscous dissipation on electromagneto-hydrodynamic flow in a microchannel with electroosmotic effect: enhancement of MEMS cooling*.– Proceedings of the Institution of Mechanical Engineers, Part N: Journal of Nanomaterials, Nanoengineering and Nanosystems, https://doi.org/10.1177/23977914231217929.

[32] Tzou D.Y. (1997): *Macro-to Microscale Heat Transfer*.– Taylor & Francis, Washington, DC

[33] Adeosun A.T., Kasim A.R.M., Khan I., Tijani Y.O. and Akolade M.T. (2025): *Bifurcation and sensitivity analysis of a convectively heated squeezed MHD hybrid nanofluid with nonlinear radiation: a spectral approach*.– Computers & Mathematics with Applications, vol.195, pp.28-41, https://doi.org/10.1016/j.camwa.2024.12.025.

Received: December 6, 2025
Revised: May 7, 2026